Single-Molecule Fluorescence Microscopy Reveals Local Diffusion Coefficients in the Pore Network of an Individual Catalyst Particle

Frank C. Hendriks, Florian Meirer, Alexey V. Kubarev, Zoran Ristanović, Maarten B.J. Roeffaers, Eelco T.C. Vogt, Pieter C.A. Bruijnincx, and Bert M. Weckhuysen

Supplementary information

S1. Experimental details

In situ cell used in single molecule fluorescence experiments. The in-situ cell consists of a metal holder in which a glass plate with particles is placed. The glass plate is lined with a PMMA seal and a PTFE liner making up the walls of the cell; the overall assembly is held in place by two screws (Figure S1).
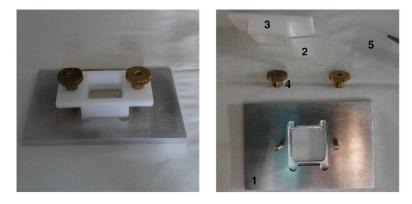

Figure S1. In-situ cell used in experiments with (1) metal holder; (2) PMMA seal; (3) PTFE lines; (4) screws and (5) glass plate.

Sample preparation. The FCC catalyst particles, containing ZSM-5 as the active zeolite phase, were provided by Albemarle Catalyst Company B.V. The particles were first calcined at 823 K for 72 h (ramp = 10 K/min) in a static oven to remove residual fluorescent impurities. The particles were suspended in MilliQ water and spin coated onto a glass plate. The glass plate containing the particles was then calcined for at 773 K for 48 h (ramp = 1 K/min) in a static oven.

Probe molecule. The probe molecule N,N'-bis (2,6-dimethylphenyl)-perylene-3,4,9,10-tetracarboxylic diimide (PDI) was purchased from Aldrich. PDI is a highly fluorescent and highly photostable dye that has an absorption maximum at 525 nm.[1] The emission spectrum after excitation using a 514 nm laser is shown in Figure S10b. The probe molecule was diluted to 3.3×10^{-10} M in toluene. For the experiment, 100 µL of this solution were added to FCC particles suspended in 400 µL of toluene, leading to a final concentration of 6.7×10^{-11} M.

Experimental setup. Single molecule tracking experiments were performed on a custom-made setup. An inverted epi-fluorescence wide-field microscope (Olympus IX-71) with a 100× oil immersion objective (NA=1.4) was used. A diode-pumped solid-state laser (Excelsior 532 single mode 200 mW, Spectra-Physics) provided 54 mW to the sample. Fluorescence images were recorded as movies using a Hamamatsu ImagEM X2 C9100-23B EM-CCD camera, after passing through a dichroic mirror, a 3.3× camera lens and a 600/60 band pass filter. The resulting field of view was $24.6 \times 24.6 \ \mu m^2$ and $48.5 \times 48.5 \ nm^2$ per pixel (512×512 pixels).

Experiment. The experiment was performed at room temperature (294 K). A powerful laser is used to illuminate the sample, so some increase in temperature of the toluene suspension cannot be excluded. However, no significant evaporation of the solvent was observed, nor any visual signs of heating of the suspension. After addition of the probe molecule, the system was left to equilibrate for 5 min. In the course of 2 h, 7 movies were recorded with a total of 63,000 frames. There is a slow increase in the number of tracks over time; other than that, the movies show no observable differences.

Analysis. Detection of single molecule events and subsequent track analysis was done using the Localizer plug-in of Igor Pro.[2] For track analysis, molecules were allowed to blink (i.e. the molecule does not fluoresce intermittently) for 1 consecutive frame.[3] Track classification, analysis and plotting was done in MATLAB. It was found that some of the tracks have negative D values; this (physically impossible) result stems from erroneous fitting of mean square displacement curves and these values were therefore discarded. No tracks are observed outside of the particle, because molecules in solution move too fast to be registered under the experimental conditions applied and analysis parameters used.

Drift correction. Some intra- and inter-movie drift was indeed detected. Inter-movie drift (i.e. a shift in the location of the particle between the end of one movie and the start of the next) was corrected for by aligning (rigid shift in x and y) individual movies in a global coordinate system. The shift was determined by comparing the center of the convex hull of the particle (the area including all detected events) in consecutive movies. Intra-movie drift (i.e., drift while the movie is begin recorded) was observed in some movies in the form of a slow, continuous drift. This was difficult to remove, especially because the moving probe molecules inside the catalyst provide no frame of reference for drift. However, because is was a slow and small drift during one movie resulting in a very small displacement between individual frames, we estimated that the average error to track analysis introduced by intra-movie drift, in a movie with

10.000 frames, was below 1 nm (i.e. well below our localization uncertainty). Therefore, we did not analytically address this type of drift further.

S2. Single Molecule Events

Figure S2 a shows a zoom-in of one frame of a single molecule movie. Clearly visible is a single molecule event (white). Two single molecule tracks detected in this region are shown in blue and red. The integrated intensity of the region of interest (white dashed-line square) is shown in Figure S2b, where the higher intensity caused by the single molecule event can be distinguished for both tracks. In Figure S2b, between the higher intensity of the two tracks, two frames with low intensity are observed. The algorithm therefore identifies two separate tracks. These two tracks may well be from the same PDI probe molecule, that has for example moved out of focus for two frames. However, it can also not be excluded that these tracks are from two different molecules.
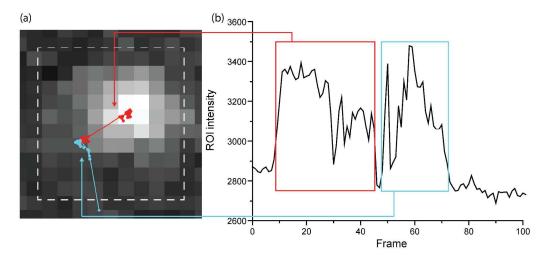

Figure S2. Intensity trace of two tracks in the same area. (a) Single molecule event from one of the tracks. (b) Intensity trace integrated over the complete ROI (indicated by white dashed-line square).

S3. Frame length

The duration of one frame is set at 20 ms but deviates from this value because the detector reads out the data from one frame before it can start the next. The frame length for each frame was calculated from the time stamp of the individual frames and is plotted in Figure S3. There is a narrow distribution of frame lengths; the observed difference is 0.2 ms. Some outliers are observed but these are likely caused by a delay in writing the time stamp. There is no shift of frame duration over time. Therefore, the average frame duration over the whole movie was used in further calculations, which is 20.300 ms (49 frames/s).
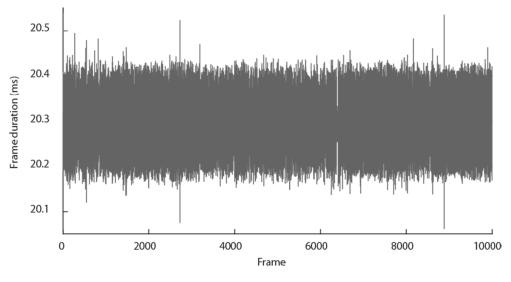

Figure S3. Fluctuations in the average frame duration in a movie of 10,000 frames.

S4. Projection of 3D movement onto 2D plane

The analysis does not consider the position of the emitter in the Z-direction. Movement is therefore considered to be a projection of a sphere onto a plane, leading to an underestimation of the actual movement.[4] We have simulated this by considering 10,000 unit vectors from the origin pointing in random directions in 3D. Therefore, all resulting vectors end on the surface of a unit sphere (Figure S4a). The vectors were then projected onto 2D space, i.e. a unit circle (Figure S4b). A histogram of the resulting vector lengths is reported in Figure S4c showing the error introduced by projecting a 3D movement of unit length onto a 2D plane. Considering the average of a large number of movements the error introduced by this projection is relatively small, with the average measured vector length in 2D being 0.78 (± 0.22) × the vector length in 3D.
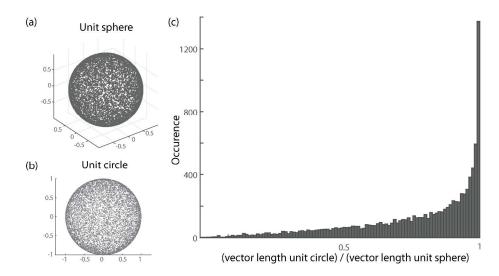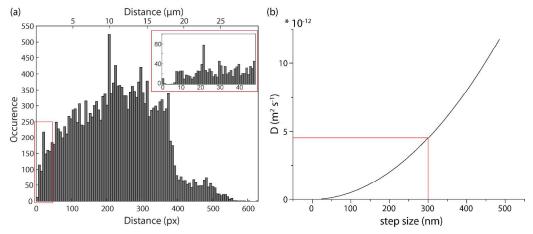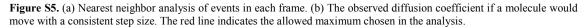
Figure S4. (a),(b) A graphical representation of random 3D movement with each point on the surface of the unit sphere signifying the endpoint of a vector pointing from the center of the sphere to that point on the surface (a). The same unit sphere projected onto a 2D surface (b). c) A histogram of the resulting vector lengths measured from the 2D projection.

S5. Analysis of single molecule events

For track analysis, it is important to know the chance of false positives, i.e. the chance of having two molecules in close proximity that do not belong to the same track. To this end, a nearest neighbor analysis was carried out on all events within each frame (Figure S5a). In a single frame the events are independent (stochastic) and can be used to calculate the probability of two single molecule events in close proximity (events in consecutive frames are themselves not independent as they could be originating from the same molecule). The histogram shows there is a sharp increase in events that are more than 6 pixels (291 nm) apart from each other, which is the reason this step size was chosen as the maximum allowed in track analysis. Figure S5b shows that a molecule that would move with the maximum step size consistently would have a diffusion coefficient of $\sim 5 \times 10^{-12}$ m^2 s^{-1}.

Figure S5. (a) Nearest neighbor analysis of events in each frame. (b) The observed diffusion coefficient if a molecule would move with a consistent step size. The red line indicates the allowed maximum chosen in the analysis.

S6. Track direction

We detected an increase in the number of tracks as the experiment progressed. This could imply that a concentration gradient was present within the particle and equilibrium had not been reached. A concentration gradient would cause directed diffusion of the molecules, and in order to check for the presence of any superimposed directed diffusion that would influence the direction of the tracks, the angle of the first eigenvector of each track (indicating the principal direction of a track) with respect to the center of the particle was plotted. However, no preferential direction of tracks inside the particle was detected.

By analyzing the location of the tracks, it was found that the increase of tracks was mainly located at the edge (surface) of the particle. In the center, the density of tracks was almost constant. This implies molecules had penetrated to the middle of the catalyst particle before the experiment started. We therefore speculate that the increasing number of tracks at the edge of the particle may be caused by the dense crust around the FCC catalyst particle (see main text).
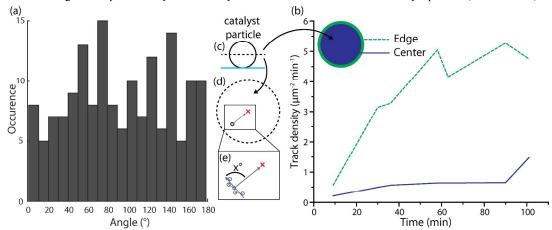

Figure S6. (a) Histogram of the angle between the track eigenvector and the vector pointing to the particle center calculated for each mobile track (see also (c),(d),(e)). The absence of a preferential angle shows that there was no directed movement of tracks towards the center of the particle, providing evidence that molecule diffusion was not influenced by a concentration gradient. (b) The track density as a function of time. Tracks within $1/8 \times r$ from the surface were considered to be tracks at the edge of the particle; the rest was considered to be in the center. The discrete times shown are deducted from the time stamp of the individual movies (see S1); to obtain track density the number of tracks was divided by the area of the edge/center and divided by the duration of the movie. (c) The FCC catalyst particle used in the experiment; the blue line indicates the glass bottom plate of the in-situ cell. The dashed line indicates the center plane at which the main experiment was measured. (d) Schematic of the center plane showing the center of the particle (marked with an ×) and one track (marked with a circle). (e) a zoom-in of the area, showing the first Eigenvector of the track (which indicates its principal direction) and the vector from the center of mass of the track to the center of the particle, both marked with gray arrows. The angle between these two is shown in the histogram in (a).

S7. Machine learning

To apply machine learning as a tool for automated track classification, several tracks first had to be classified by hand. A 'training set' of 100 tracks was classified manually. Based on the similarities in track properties in each subgroup, the algorithm is then able to group a large set of tracks following a decision tree built from the training set. The list of properties shown below was used for generating the decision tree shown in Figure S7. In order to filter immobile tracks the decision tree was extended by the purple part shown in Figure S7 using a condition based on the diameter of the smallest enclosing circle. This condition is based on a priori knowledge of the setup (the localization uncertainty) and can therefore not be automated. The total number of tracks is relatively small in this case, and could in principle be sorted manually. However, the developed methodology can be applied to a dataset regardless of its size. Moreover, if the appropriate properties are chosen, a wide range of possible track types can be identified, not just the track types distinguished here.

Although the track types are clearly defined, the differences between tracks are sometimes minimal. For example, as shown in Figure S10a, there is no clear distinction between steps that fall within the localization uncertainty and steps associated with actual molecular movement. Therefore, the machine learning algorithm does not perfectly separate tracks; the zoomed-in area in Figure 2 (main text) provides some examples. However, from the results obtained in the subsequent analysis of the average properties of the subsets such as the diffusion coefficient D, it can be concluded the obtained classification was sufficient for this study.

List of track properties

a. Number of steps

   Number of consecutive single molecule emitters detected.

b. Diameter of the smallest enclosing circle

c. Center of the smallest enclosing circle

d. Center of mass based on all points of a track

e. Distance between c and d

   The distance between the center of the smallest enclosing circle and the center of mass based on all points gives an indication of how points are distributed spatially. It is calculated as a percentage of the track's diameter (b).

f. Length

g. Tortuosity

   The ratio of the distance between start and end point versus the length of the track.

h. Entropy

   A statistical measurement of randomness applied to the distribution of the points within the enclosing square that is defined by the smallest enclosing circle.

i. Diffusion coefficient

   This is the diffusion coefficient as calculated from the fit of the mean square displacement graph of the track.
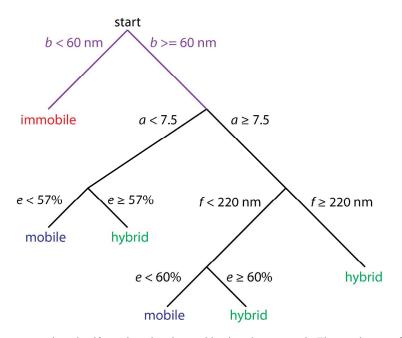

Figure S7. Decision tree used to classify tracks using the machine learning approach. The purple part of the tree has been added manually (by setting a threshold for the diameter of the minimum enclosing circle based on the localization uncertainty), while the part of the tree plotted in black was created automatically by the machine-learning algorithm. During classification of all tracks, for each track, the decision tree is followed from top to bottom, weighing one property at each branch, until the track is classified as either mobile, immobile, or hybrid.

S8. Fluorescence attenuation by the catalyst particle

Because the middle section of a whole spherical FCC particle is measured, the emitted fluorescence intensity is influenced by the location at which it is recorded. Due to the spherical shape of the particle, fluorescence must travel through a varying amount of material to reach the detector; the same is true for the incident light (see Figure S8c). The material can scatter or absorb the light, leading to lower observed fluorescence intensity. To study any possible effect of this absorption on the detected track density, the influence of fluorescence attenuation was investigated.

The intensity distribution of events at two different depths (5 and 10 μm) was measured and fitted using a Gaussian function (quality of fit parameter R^2 = 0.9647). From the shift and reduced sigma observed between the intensity distributions recorded at these two depths (x_1 and x_2), the characteristic fluorescence intensity attenuation coefficient μ at the recorded wavelengths (~500-600 nm) and for the FCC catalyst particle was calculated using Beer-Lambert's law[5] $I = I_0 \cdot e^{\mu \cdot x}$. To verify this approach, we simulated the effect of fluorescence intensity attenuation at different depths in a material causing a shift and reduced sigma of a normal distribution of fluorescence intensities: a simulated intensity distribution as it would be detected at the surface of the particle (i.e. without any intensity attenuation) can be seen in Figure S8b (orange histogram). The green and blue intensity distributions were then calculated being this exact same distribution but with the intensity of each fluorescence event attenuated following Beer-Lambert's law, i.e. as a function of depth x into the material and an arbitrarily chosen attenuation coefficient μ. From the known depths x and the shift and reduced sigma obtained from a fit to the intensity distributions the actual attenuation coefficient μ (which is a material constant) can then be recovered.

Following this approach and using the experimental data the attenuation coefficient μ for the FCC catalyst was found to be 0.094 μm^{-1}. (The data was also fitted using a lognormal function instead of a Gaussian, as this seemed to fit the tail of the distribution better.[6] Not surprisingly this gave a very similar result, i.e. an attenuation coefficient μ of 0.085 μm^{-1} (R^2 = 0.9191), because μ is determined from the shift between the distribution functions and therefore not directly related to the shape (i.e. nature) of the distribution function. The difference in μ obtained from using a Gaussian and lognormal function is only caused by a slightly different shift obtained when using different distribution functions.) With this μ, the expected absorption by the material in the middle section of the FCC particle (i.e. the section that was used for the track analysis) was calculated.

The results of this approach are summarized in Figure S8d. The red line indicates the expected decrease of events at the center plane of the catalyst particle (i.e., the plane that was measured in our main experiment) from the surface towards the middle of this plane. The histogram shows the actual number of tracks found. Although attenuation of fluorescence accounts for a decrease in tracks towards the middle of the particle, this is clearly not the only influence (see main text).
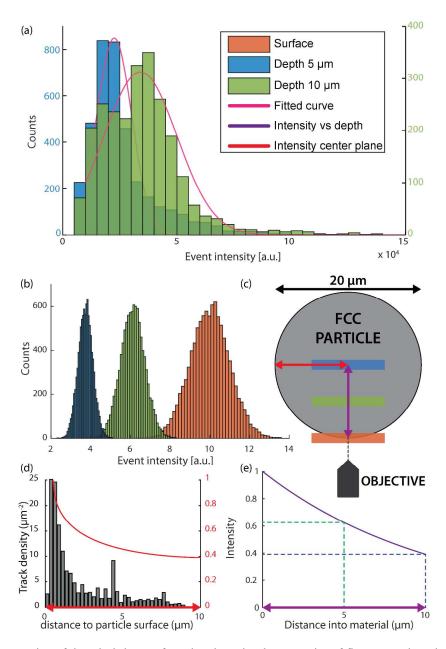
Figure S8. An overview of the calculations performed to determine the attenuation of fluorescence intensity by the FCC particle. (a) Histogram of intensities of events at 2 different depths (green = 5 µm; blue = 10 µm into the particle), including a Gaussian fit of both histograms. From these depths, only events within 5 µm from the center were selected to account for the curved surface of the particle and obtain almost constant optical path lengths (see (c)). (b) Simulated normal distributions of event intensity at the surface (orange) and at depths of 5 and 10 µm. (c) Scheme explaining the locations of the intensity distributions within the FCC particle. (d) Track density as a function of distance from the surface of the FCC particle; in red the exponential decay of fluorescence intensity based on absorption coefficient determined for the material. (e) Intensity as a function of depth into the particle.
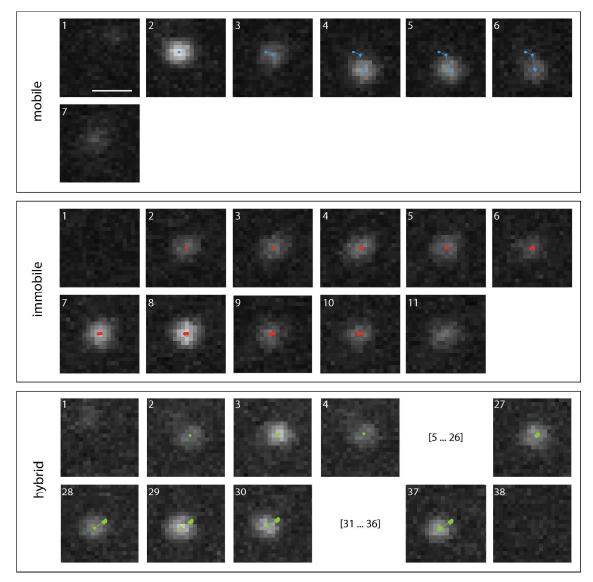
S9. Track types and their properties

Figure S9. Close-up images of each type of track encountered within the recorded movies. Localized positions are denoted by dots, with lines showing the track evolution. The first and last frames in each series show the same area before and after events were detected. The scale bar represents 0.5 μm and applies to all images. Intensities have arbitrary units and are the same across all images.

The most distinct properties of each track type are shown in Figure S10. The histogram of step sizes (Figure S10a) shows that while immobile tracks obviously have the smallest steps, hybrid and mobile tracks each also have a significant number of small steps, indicating that most molecules spend at least a short time in the immobile state (or move along the z-axis, see Figure S4). Figure S10b shows that the number of points for mobile tracks on average is low, which is likely caused by out-of-focus movement of these tracks. In Figure S10c, the diameter of the smallest enclosing circle of the tracks from the experiment with PDI molecules immobilized in polystyrene is also shown. There is a strong overlap with the histogram of the immobile tracks, providing evidence that the immobile tracks really are immobile.
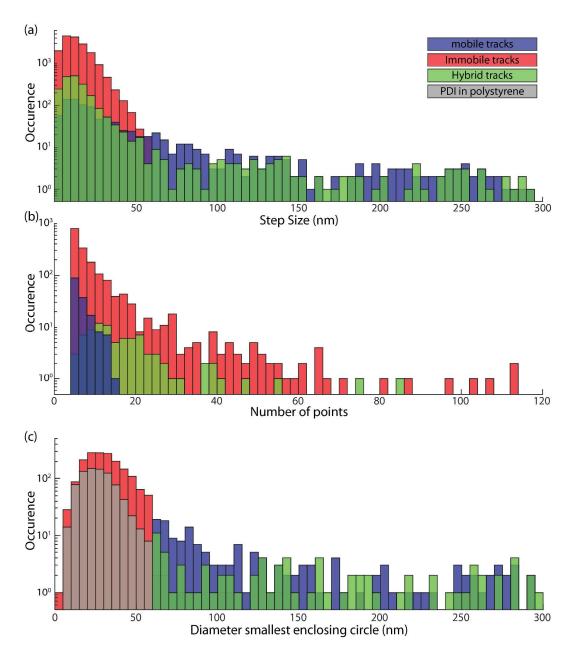
Figure S10. Histograms of step sizes (a), the number of points (b) and the diameter of the smallest circle enclosing all points of a track (c). The colors of each type of track are given in the legend; overlapping bars produce different colors (e.g. blue and red combine to purple in (a) and (b)).

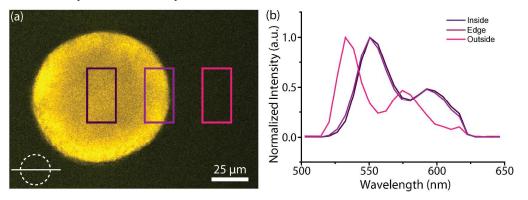## S10. Emission spectrum of PDI probe molecule

Figure S11. a) Confocal fluorescence microscopy image of the probe molecule PDI in an FCC particle, with a region of interest in the middle of the particle (purple), at the edge (violet) and outside of the particle, in the solution (pink). The image is recorded at the center plane of the particle (see scheme). The image is recorded using a confocal fluorescence microscopy equipped with a spectral detection unit and using 514 nm laser light for excitation. b) Spectra corresponding to the ROIs in a), with normalized intensity.

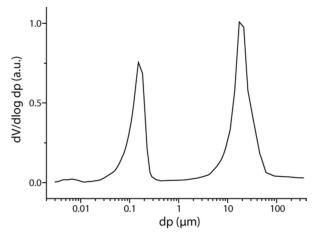## S11. Mercury Porosimetry on FCC particles

Figure S12. Bulk mercury porosimetry results of the FCC catalyst material under study. The peak at 10-50 µm corresponds to the interparticle space. Therefore, the porosimetry results show that most of the macropores range from 50-300 nm in size.

S12. Mercury Porosimetry on FCC particles

To quantify the (projected) 2-D movement of PDI in the particle, the mean square displacement (MSD) as a function of time lag τ was calculated for each track (Figure S13). In this calculation, each intermediate position of a track is considered a valid starting point for calculating the MSD, rather than looking at each track from start to finish.[7] The three track types show clear differences in their MSDs. Notably, the mobile and hybrid tracks show a broad distribution in MSD offset values. With displacement being directly related to a molecule's confinement, this broad MSD distribution can therefore be considered a consequence of the large range of pore sizes present within the FCC catalyst particle (Figure S12).[8]
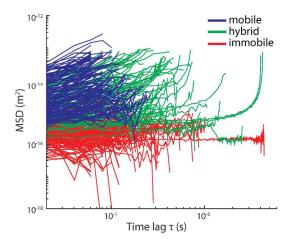

Figure S13. The individual mean square displacement (MSD) of each detected track as a function of time lag τ, with immobile tracks in red, mobile in blue and hybrid ones in green. Only 10% of the immobile tracks are shown for clarity. Please note that this is a log-log plot; the time lag τ starts at 2×10^{-2} s, corresponding to the framerate.

S13. Radial distribution of diffusion coefficients

To test for a correlation between diffusion coefficient D and the depth into the particle at which a molecule is present, the average diffusion coefficient was plotted for three depths within the particle cross-section (Figure S13b). Zone A is > 6 µm into the particle, B is from 3 to 6 µm into the particle, while C is < 3 µm into the particle. The diffusion coefficients of mobile and hybrid tracks were used, as the immobile tracks have diffusion coefficients that cannot be distinguished from the localization uncertainty. Using a statistical t-test, no significant differences were found between the diffusion coefficients in the three zones (Figure S13c).
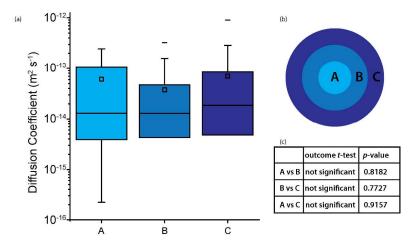

Figure S14. a) Box plots of the average diffusion coefficient within three different depths into the particle. The mean value is marked by '□'; the maximum value is marked by '-'. b) Legend indicating the zones at different depths within the FCC particle cross section. c) Statistical t-tests carried out on the subsets.

S14. Calculating the Thiele modulus and effectiveness factor

The Thiele modulus ϕ_2 and effectivity η for a second order reaction can be calculated by the following formula:[9,10]

$$\varphi_2 = r \cdot \frac{1}{3}\sqrt{\frac{k \cdot C_s}{D}} \qquad\qquad \eta = \frac{\tanh \varphi}{\varphi}$$

The conversion process for FCC itself was approximated by the cracking of cetane (C_{16}) to octane (C_8); therefore, one cracking event per feed molecule is assumed as well as 100% conversion.[11] For the FCC process, 40×10^3 kg catalyst circulates through the reactor per minute.[12] Each minute, 7×10^3 kg of feedstock is converted. The residence time is 1 second. This leads to a rate k of 1.93×10^{-2} mol L^{-1} s^{-1}. The diameter of an FCC catalyst particle was approximated to be 75 µm. For the concentration of feedstock at the catalyst's surface C_s, a monolayer coverage of reactants (cetane) was used on the outside of the spherical catalyst particle (2.57×10^{-4} mol L^{-1}). The diffusion coefficient D for mobile tracks (7.73×10^{-14} m^2 s^{-1}) was used, but a conversion factor (5.25×10^3) was used to correct for the difference in temperature between the experiment (294 K) and the real process (800 K).[11] The conversion factor used was based on the work by Vasenkov and Kärger.[13]

S15. Van Hove diagram

The existence of different types of movement is evident from the distribution of displacements after time lag τ (the van Hove correlation function, Figure S14), a clear deviation from a normal distribution (red line) is observed.[14,15] The exponential tail indicates a small subset of molecules showing different diffusion characteristics than the rest of the tracks, in this case the mobile tracks. This has been observed before in heterogeneous systems, such as quantum dots in polyacrylamide gels.[16]
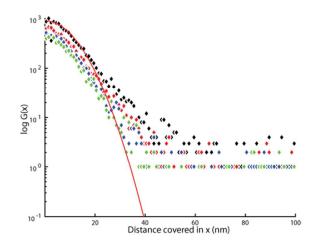

Figure S15. Van Hove correlation graph showing the probability of tracks having travelled certain distances after a time lag of 5 (black), 10 (red), 15 (blue) and 20 frames (green).

References

(1)   Rademacher, A.; Märkle, S.; Langhals, H. *Chem. Ber.* **1982**, *115*, 2927.

(2)   Dedecker, P.; Duwé, S.; Neely, R. K.; Zhang, J. *J. Biomed. Opt.* **2012**, *17*, 1.

(3)   Vogelsang, J.; Steinhauer, C.; Forthmann, C.; Stein, I. H.; Person-Skegro, B.; Cordes, T.; Tinnefeld, P. *Chemphyschem* **2010**, *11*, 2475.

(4)   von Diezmann, A.; Shechtman, Y.; Moerner, W. E. *Chem. Rev.* **2017**, *117*, 7244.

(5)   Lambert, J. H. in *Photometria, sive de Mensura et Gradibus Luminis Colorum et Umbrae*; Augsburg, 1760.

(6)   Kish, L. L.; Kameoka, J.; Granqvist, C. G.; Kish, L. B. *Appl. Phys. Lett.* **2011**, *99*, 143121.

(7)   Hellriegel, C.; Kirstein, J.; Bräuchle, C.; Latour, V.; Pigot, T.; Olivier, R.; Lacombe, S.; Brown, R.; Guieu, V.; Payrastre, C.; Izquierdo, A.; Mocho, P. *J. Phys. Chem. B* **2004**, *108*, 14699.

(8)   Kirstein, J.; Platschek, B.; Jung, C.; Brown, R.; Bein, T.; Bräuchle, C. *Nat. Mater.* **2007**, *6*, 303.

(9)   Wallenstein, D.; Fougret, C.; Brandt, S.; Hartmann, U. *Ind. Eng. Chem. Res.* **2016**, *55*, 5526.

(10)   Stockwell, D. M. In *Fluid Catalytic Cracking VII: Materials, Methods and Process Innovations.*; Occelli, M. L., Ed.; Elsevier: Amsterdam, 2007; p 137.

(11)   Froment, G. F.; Bischoff, K. B.; Wilde, J. De. In *Chemical Reactor Analysis and Design*; John Wiley & Sons: New York, 2011; p 720.

(12)   Gary, J. H.; Handwerk, G. E.; Kaiser, M. J. In *Petroleum Refining: Technology and Economics*; CRC Press: New York, 2007; p 115.

(13)   Kärger, J.; Vasenkov, S. *Micropor. Mesopor. Mat.* **2005**, *85*, 195.

(14)   Kegel, W. K. *Science* **2000**, *287*, 290.

(15)   Van Hove, L. *Phys. Rev.* **1954**, *95*, 249.

(16)   Lee, C. H.; Crosby, A. J.; Emrick, T.; Hayward, R. C. *Macromolecules* **2014**, *47*, 741.